
Study of instabilities generated by a rotating ellipsoid embedded in a stratified fluid

Camille-Lucia CATHALAN

* Supervised by Antoine CHAUCHAT and Michael LE BARS *
December 2023

L3 MPC I Internship - Year 2023-2024

Contents

1	Introduction	1
1.1	General context	1
1.2	Goals of the internship	2
1.3	Laboratory presentation	2
2	Theoretical approach	3
2.1	The backdrop: a stratified medium in the Boussinesq approximation	3
2.1.1	Stratification	3
2.1.2	Boussinesq approximation for buoyancy	3
2.2	Flow generated by a sphere rotating in a stratified fluid	4
2.2.1	Forces involved	4
2.2.2	Resolution for velocity	5
2.2.3	Resolution for density	5
2.3	Internal gravity waves	6
2.3.1	Brunt-Väisälä frequency	6
2.3.2	Properties of internal gravity waves	8
2.4	Instabilities	9
2.4.1	Centrifugal instabilities	9
2.4.2	Double-diffusive and viscous-diffusive instabilities	9
2.4.3	Convective instability	9
3	Experimental work	10
3.1	Experimental setup	10
3.2	Particle Image Velocimetry	10
3.3	Experiment zero: stratification elaboration with the double-bucket method	10
3.4	First experiment: velocity settling	12
3.4.1	Experiment 1: velocity settling without tank rotation	12
3.4.2	Experiment 2: measurement of the velocity settling with a rotating tank	13
3.5	Instabilities study	14
3.5.1	Dimensionless numbers	14
3.5.2	Criteria for meddies' instability beginning	15
3.5.3	Second experiment: measurement of instabilities in the flow without tank rotation	15
3.6	General results and discussions	16
4	Conclusion	19
5	Appendix	20
5.1	Organisation chart	20
5.2	Nomenclature	21
5.3	Detailed calculation of p	21
5.4	Dedalus solver: spectral method for numerical simulations	22
5.5	PIV examples	22
	References	25

Acknowledgements

First of all, I wanted to thank Antoine CHAUCHAT, my supervisor, which introduced me with a lot of perseverance to his enthralling PhD research theme across this training.

I also wanted to thank Michael LE BARS, my other supervisor, researcher at the IRPHE to have made this training possible, welcoming me in his team with great kindness.

Many IRPHÉ PhD students spent time to present their experiments, answer my questions, and share with me accounts of their everyday life as young researchers. I wanted to thank in particular Louise TERRIEN, Lucas GEY, Valentin DOREL, Florian REIN and and Marine AULNETTE, and more broadly, all the IRPHÉ members I could exchange with.

I sincerely express my gratitude to Julien DESCHAMPS, researcher at the IRPHÉ and teacher in MPCl bachelor degree, for having helped me to get an internship at the IRPHÉ.

This training would not have taken place without the MPCl bachelor degree internship supervisor Guillaume MAIRE. In addition to the training's advices and administrative preparation, the monitoring throughout December has been beneficial to help us dealing with deadlines.

Eventually, I would like to thank my reporter, Pr. Marc GEORGELIN, for the time he will devote for this report, and hope he will find it interesting.

Chapter 1

Introduction

1.1 General context

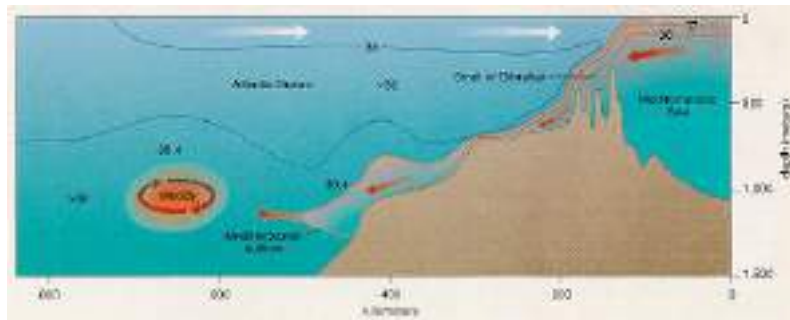
In a climate change context, oceans play a major role in absorbing excess carbon dioxide and heat in Earth's energy budget. However, this absorption capacity is not well known since these fluxes between ocean and atmosphere depend on the vertical mixing of the oceans, which is not totally understood yet. The measured vertical mixing rate is ten times smaller than the one expected to balance oceans' energy budget [6]. Local mixing mechanisms are a way to explain this.

Mediterranean eddies, or *Meddies*, are oceanic vortices formed by hot and salty water passing from Mediterranean sea to the Atlantic Ocean through the Strait of Gibraltar, as presented on fig. 1.1. The Atlantic Ocean is stratified due to its higher density so this salty water sinks until it reaches the depth at which its density matches the density of the Atlantic Ocean, forming a water lens. Then, Earth's rotation puts it in a rotating motion by effect of the Coriolis force. Meddies have usually dimensions around 40 to 100 km in diameter and are 500 to 1000 m thick at their core [11, 15].

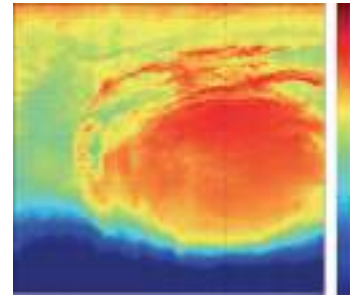
The reason why these lenses of salt water attract so much attention is that they help to redistribute heat and salt in a significant way [13]. Moreover, meddies may have an important role in mixing the oceans as they generate instabilities that can contribute to improve vertical motion of particles, nutrients and energy. These instabilities have been numerically studied in [19] for instance.

Furthermore, structures similar to meddies can be found in wildfire plumes, meteorology or planetary science. For instance, Jupiter's Great Red Storm could be a kind of meddy [11].

Understanding instabilities generated by meddies could therefore help scientists to better understand their mixing properties and eventually the impact they have on their neighbourhood.



(a) Meddies' setting up mechanism. The meddy is coming from the Mediterranean outflow, saltier and therefore denser than the surface water of the Atlantic Ocean. Taken from [15]



(b) Acoustic view of temperature field revealing a meddy. The picture shows perturbations at the boundary between the meddy and the ocean. Taken from [12]

Figure 1.1: An overview of meddies

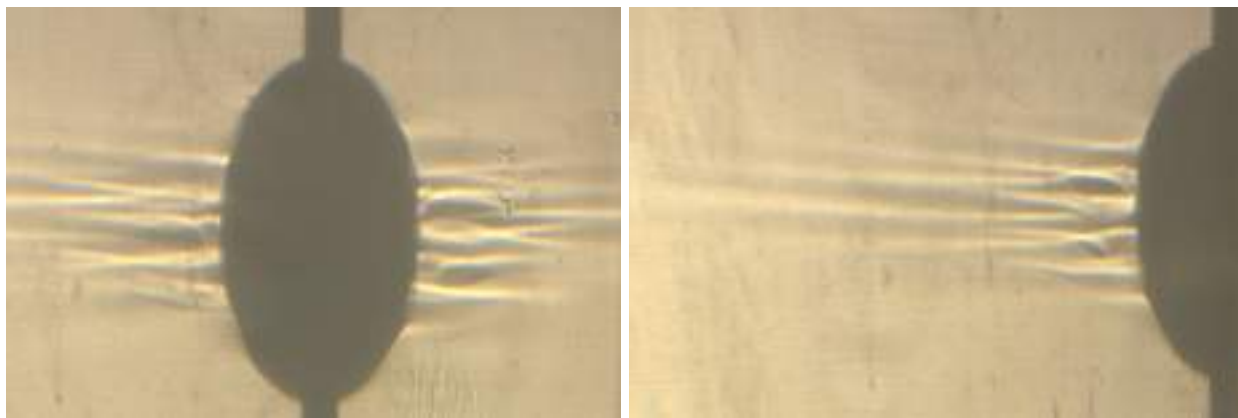


Figure 1.2: Instabilities at the sphere’s equator. Obtained by shadowgraphy, a technique which consists here in projecting the enlightened sphere on a white screen. Light is deviated depending on the refractive index of the water, which varies with density.

1.2 Goals of the internship

This training aims to improve the understanding of the instabilities caused by meddies. Assuming that a meddy has a similar behaviour to a solid sphere, we can see in fig 1.2 an instability pattern on which investigate. To do so, both theoretical and experimental studies will be conducted. Firstly, we will present the modelling of a stratified fluid at mesoscale, the concept of internal waves, and solve flow and density equations for a solid spherical meddy rotating in the ocean. Secondly, we will introduce the experimental setup and the performed experiments, and discuss the obtained results in light of the theoretical ones obtained in the previous chapter. We will also use this chapter to define some dimensionless numbers which will serve for the introduction of an instability criterion. Eventually, we will conclude by summarising the obtained results and suggest some further investigations.

1.3 Laboratory presentation

The *Institut de Recherche sur les Phénomènes Hors-Équilibre* [16], is a mixed research institute (UMR 7342) involving the *Centre National de la Recherche Scientifique*, Aix-Marseille University and the *École Centrale Méditerranée*, which conducts research on multidisciplinary topics entailing fluid mechanics.

It involves around 80 people in various positions, including 11 researchers, 22 university lecturers and researchers, 25 PhD students, 7 post-doctoral researchers and 15 engineers, technicians and administrative agents. The organisation chart is provided in appendix 5.1.

Research fields explored are divided in four main axes which are:

- Industrial flows, with the study of rotors, turbomachines and wakes generated by obstacles;
- Materials and industrial processes, with for instance the study of jets and reactive fronts, combustion, solidification;
- Living matter and biological systems which includes topics such as blood circulation, tree structure and swimming models;
- Environment and Universe, in which are studied stratified environments, inertial instabilities, waves and tsunamis, and erosion for example.

To support all the conducted experiments, the laboratory is equipped with a design office and a mechanical manufacturing workshop.

The laboratory is in partnership with many industrial organisations such as the IRSN (*Institut de radioprotection et de sûreté nucléaire*), the IRSTEA (*Institut national de recherche en sciences et technologies pour l’environnement et l’agriculture*) and Airbus Helicopters. At the international level, it collaborates with ten or so universities, and regularly receives researchers from other laboratories.

Chapter 2

Theoretical approach

In this chapter, we present some concepts involved in the training's performed experiments. Firstly, we will present the background of our research subject, introducing stratification and Boussinesq approximation. This approximation will then be used to solve the base flow equations for a rotating sphere in a stratified fluid.

Secondly, we will introduce a particular type of waves, internal gravity waves, which will be a first step in the study of the misunderstood perturbations observed in the experimental setup.

To conclude this chapter, we will present different types of instabilities.

2.1 The backdrop: a stratified medium in the Boussinesq approximation

2.1.1 Stratification

As this training has to do with stratified fluids, we must first of all define what we mean by that. Stratified fluids are fluids which move in horizontal layers because their density varies in the vertical way [18, 7]. This horizontal layering leads to inhibited vertical motion, in order to minimise fluids' internal energy.

An example of stratification is given in fig. 2.2. As it will be described in the experimental chapter, a linear stratification has been used in the middle of the fluid: the tangent to the curve fits well the points on about 30 cm.

Some types of stratification are unstable such as boiling water in a pan [18], where hot water rises and fresh water sinks, in a convection motion. During this internship, we will not consider this case, and will rather focus on stably stratified fluids, which better depict oceans' behaviour. In this case, surface water is indeed warm due to solar energy, and stays at the top of the stratification due to its lower density, conducting to a stable stratification.

2.1.2 Boussinesq approximation for buoyancy

Boussinesq approximation is a frequent approximation in fluid mechanics, that applies to fluids with a little varying density over the depth [18]. It consists in neglecting all variations in ρ , except if multiplied by g , the acceleration due to the gravity. This approximation is relevant for oceans since density varies only by a few percent from the surface to the seabed [18].

The Navier-Stokes equation

$$\frac{\partial \vec{u}}{\partial t} + (\vec{u} \cdot \nabla) \vec{u} = -\frac{1}{\rho} \nabla p + \nu \nabla^2 \vec{u} + \frac{1}{\rho} (\vec{F} + \rho \vec{g}) \quad (2.1)$$

consequently becomes

$$\frac{\partial \vec{u}}{\partial t} + (\vec{u} \cdot \nabla) \vec{u} = -\frac{1}{\rho_0} \nabla p + \nu \nabla^2 \vec{u} + \frac{1}{\rho_0} (\vec{F} + \rho \vec{g}) \quad (2.2)$$

Where $\frac{\partial \vec{u}}{\partial t}$ is the time dependence of the motion, $(\vec{u} \cdot \nabla) \vec{u} = (\nabla \vec{u}) \cdot \vec{u}$ is the convection term, $\nu \nabla^2 \vec{u}$ the diffusion term and \vec{F} the external volumic density of forces (different than weight) acting on the system.

Considering the continuity equation $\frac{\partial \rho}{\partial t} + \nabla \cdot (\rho \vec{u}) = 0 \iff \frac{\partial \rho}{\partial t} + \rho \nabla \cdot \vec{u} + \vec{u} \cdot \nabla \rho$, if the fluid is assumed incompressible (implying that $\nabla \cdot \vec{u} = 0$), the Boussinesq approximation leads to $\frac{\partial \rho}{\partial t} = 0$ and density is thus stationary.

2.2 Flow generated by a sphere rotating in a stratified fluid

In this part, equations of the flow for a sphere rotating in a stratified fluid are solved. The sphere rotates around the \vec{e}_z axis, its radius is written R and its angular velocity is referred as Ω .

In order to reproduce Earth's rotation, it is also assumed that the fluid is placed in a rotating frame with an angular velocity of Ω_T , oriented towards \vec{e}_z too.

Spherical $(\vec{e}_r, \vec{e}_\theta, \vec{e}_\phi)$ and cylindrical $(\vec{e}_{r,c}, \vec{e}_\phi, \vec{e}_z)$ coordinates are used according to the needs. It must be kept in mind that ϕ remains identical in both cylindrical and spherical coordinates, as it will help to simplify some calculations. r and r_c are the radial component in spherical and cylindrical coordinates respectively.

It is assumed that the flow is stationary, just as the fluid pressure p and the density ρ . The fluid velocity \vec{u} is assumed to verify $\vec{u} = u(r, \theta) \vec{e}_\phi$, and as the flow is axisymmetric, ρ and p have the same dependencies as \vec{u} .

2.2.1 Forces involved

The fluid here is not assumed inviscid so the viscosity term in Navier-Stokes equation must be kept.

A fluid particle is exposed to its weight, and to the fluid pressure, however, since the considered frame is no longer Galilean, two "forces", or fictitious forces¹, must be added: Coriolis force and centrifugal force.

Meddies are large structures (around 100 km radius) so Earth's rotation must be taken into account to fully understand them, hence the consideration of Coriolis force, which is expressed $\vec{f}_{Cor} = -2\rho \vec{\Omega}_T \times \vec{u}$.

Then, due to the rotation of the fluid induced by the solid sphere, centrifugal force is expressed $f_{cen} = -\rho \vec{\Omega} \times (\vec{\Omega} \times \vec{r})$.

The Navier-Stokes equation is thus written:

$$\partial_t \vec{u} + (\nabla \vec{u}) \cdot \vec{u} = -\frac{\nabla p}{\rho_0} - \frac{\rho}{\rho_0} g \vec{e}_z - 2\vec{\Omega}_T \times \vec{u} - \vec{\Omega} \times (\vec{\Omega} \times \vec{r}) + \nu \Delta \vec{u} \iff (\nabla \vec{u}) \cdot \vec{u} = -\frac{\nabla p}{\rho_0} - \frac{\rho}{\rho_0} g \vec{e}_z - 2\vec{\Omega}_T \times \vec{u} - \vec{\Omega} \times (\vec{\Omega} \times \vec{r}) + \nu \Delta \vec{u} \quad (2.3)$$

We will first focus on the equation projected along \vec{e}_ϕ to determine the velocity field.

Terms are calculated individually. Firstly, $\nabla \vec{u} = \begin{pmatrix} 0 & 0 & -\frac{1}{r} u \\ 0 & 0 & -\frac{1}{r \tan \theta} u \\ \partial_r u & \frac{1}{r} \partial_\theta u & 0 \end{pmatrix}$ as \vec{u} has no components on \vec{e}_r and \vec{e}_θ , and $\vec{u} \cdot \vec{e}_\phi$ only depends on r and θ .

Consequently, $\nabla \vec{u} \cdot \vec{u} = \begin{pmatrix} -\frac{1}{r} u^2 \\ -\frac{1}{r \tan \theta} u^2 \\ 0 \end{pmatrix}$, so the component on \vec{e}_ϕ is null.

Secondly, pressure does not vary with ϕ so the pressure gradient on \vec{e}_ϕ is also null.

Thirdly, the \vec{e}_z vector in cylindrical coordinates can be projected in spherical coordinates : $\vec{e}_z = \cos \theta \vec{e}_r - \sin \theta \vec{e}_\theta$, which has no component on \vec{e}_ϕ .

Cylindrical coordinates will be used to calculate Coriolis force.

$$\vec{\Omega}_T \times \vec{u} = \begin{pmatrix} 0 \\ 0 \\ \Omega_T \end{pmatrix} \times \begin{pmatrix} 0 \\ u \\ 0 \end{pmatrix} = \begin{pmatrix} -\Omega_T u \\ 0 \\ 0 \end{pmatrix} = -\Omega_T u \begin{pmatrix} \sin \theta \\ \cos \theta \\ 0 \end{pmatrix} \text{ switching to spherical coordinates.} \quad (2.4)$$

Here too, there is no component on \vec{e}_ϕ .

Centrifugal force in spherical coordinates gives:

$$\vec{\Omega} \times (\vec{\Omega} \times \vec{r}) = \vec{\Omega} \times \left(\Omega \begin{pmatrix} \cos \theta \\ -\sin \theta \\ 0 \end{pmatrix} \times \begin{pmatrix} r \\ 0 \\ 0 \end{pmatrix} \right) = \Omega^2 \begin{pmatrix} \cos \theta \\ -\sin \theta \\ 0 \end{pmatrix} \times \begin{pmatrix} 0 \\ 0 \\ r \sin \theta \end{pmatrix} = -r \Omega^2 \sin \theta \begin{pmatrix} \sin \theta \\ \cos \theta \\ 0 \end{pmatrix} \quad (2.5)$$

¹These are added to correct the fact that the referential is no longer a Galilean reference frame due to its rotation

Eventually, the Laplacian is null except on \vec{e}_ϕ , so equation (2.3) becomes:

$$(\vec{\Delta}\vec{u}) \cdot \vec{e}_\phi = 0 \iff \Delta u - \frac{u}{r^2 \sin^2 \theta} = 0 \iff r^2 \frac{\partial^2 u}{\partial r^2} + 2r \frac{\partial u}{\partial r} = -\frac{\partial^2 u}{\partial \theta^2} - \frac{\cos \theta}{\sin \theta} \frac{\partial u}{\partial \theta} + \frac{u}{\sin^2 \theta} \quad (2.6)$$

2.2.2 Resolution for velocity

It will be assumed that u can be decomposed in two functions of r and θ , namely $u(r, \theta) = A(r)B(\theta)$. Assuming A and B different from 0, equation (2.6) becomes

$$\frac{1}{A(r)} \left(r^2 \frac{d^2 A(r)}{dr^2} + 2r \frac{dA(r)}{dr} \right) = \frac{1}{B(\theta)} \left(-\frac{d^2 B(\theta)}{d\theta^2} - \cot \theta \frac{dB(\theta)}{d\theta} + \frac{B(\theta)}{\sin^2 \theta} \right) \quad (2.7)$$

Two equal equations of independent variables implies that the two sides of the equation are equal to a constant $C \in \mathbb{R}$.

$$A''(r) + \frac{2}{r} A'(r) - \frac{C}{r^2} A(r) = 0 \quad (2.8)$$

Moreover, velocity of the fluid system is constraint to verify a boundary condition between the fluid and the solid sphere. We use this boundary condition $u(r = R, \theta) = \Omega R \sin \theta$, the solid sphere's velocity, to determine C :

$$(2.8) \text{ for } r = R \implies 0 + \frac{2\Omega \sin \theta}{R} - \frac{C\Omega R \sin \theta}{R^2} = 0 \iff C = 2 \quad (2.9)$$

Equation on $B(\theta)$ is:

$$B''(\theta) + \cot \theta B'(\theta) + B(\theta) \left(C - \frac{1}{\sin^2 \theta} \right) = 0 \quad (2.10)$$

We verify that $B(\theta) = \sin \theta$ is solution of equation (2.10). It comes out of the boundary condition that $B(\theta) = \sin \theta$.

Coming back to $A(r)$, $r \rightarrow \alpha r$ and $r \rightarrow \frac{\beta}{r^2}$ are two functions satisfying equation (2.8), which is an second order ordinary differential equation. Consequently, every solution of equation (2.8) is a linear combination of these two functions. However, for $r \rightarrow +\infty$, $\alpha r + \frac{\beta}{r^2} \sim \alpha r$, which is nonphysical when $\alpha \neq 0$, since it states a divergent velocity field. Thus, α must be null, and applying the condition for velocity at the sphere's boundary, it is found that $\beta = \Omega R^3$.

The velocity field is finally

$$\vec{u}(r, \theta) = \Omega R \sin \theta \left(\frac{R}{r} \right)^2 \vec{e}_\phi \quad (2.11)$$

To better visualise this field, it is possible to plot it with `matplotlib` library in Python programming language. We then get fig. 2.1.

2.2.3 Resolution for density

Now that the velocity field is known, equations will be solved to deduce the associated pressure and then density. This will allow to analyse the spatial disposition of density, which is responsible for the bright-and-dark alternating bands observed, as light is deviated in different ways through the fluid.

Density will be calculated thanks to pressure, and to determine pressure, the unused equations in equation (2.3) will be projected in cylindrical coordinates.

Convection term $(\nabla \vec{u}) \cdot \vec{u}$ in cylindrical coordinates is equal to:

$$\begin{pmatrix} 0 & -\frac{u}{r} & 0 \\ \frac{\partial u}{\partial r_c} & 0 & \frac{\partial u}{\partial z} \\ 0 & 0 & 0 \end{pmatrix} \cdot \begin{pmatrix} 0 \\ u \\ 0 \end{pmatrix} = \begin{pmatrix} -\frac{u^2}{r_c} \\ 0 \\ 0 \end{pmatrix}$$

Coriolis force in cylindrical coordinates has already been calculated in equation (2.4), and as $\vec{e}_{r,c} = \sin \theta \vec{e}_r + \cos \theta \vec{e}_\theta$, we immediately obtain $\vec{\Omega} \times (\vec{\Omega} \times \vec{r}) = -\Omega^2 r_c \vec{e}_{r,c}$ for the centrifugal force.

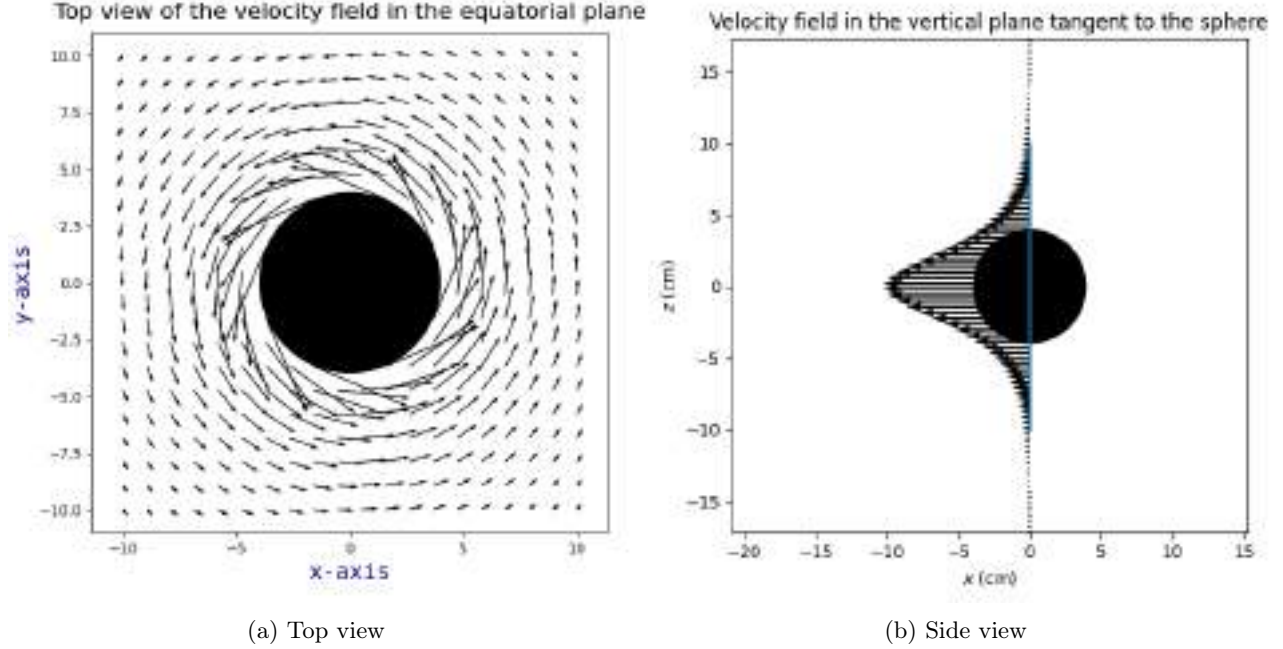


Figure 2.1: Velocity field obtained in equation (2.11): top view (2.1a) and side view (2.1b)

As before, Laplacian in cylindrical coordinates has no components neither on $\vec{e}_{r,c}$ nor \vec{e}_z . So Navier-Stokes equation (2.3) projected on $\vec{e}_{r,c}$ and \vec{e}_z becomes:

$$\begin{cases} -\frac{u^2}{r_c} = -\frac{1}{\rho_0} \frac{\partial p}{\partial r_c} + r_c \Omega^2 + 2u\Omega_T \\ 0 = -\frac{1}{\rho_0} \frac{\partial p}{\partial z} - \frac{\rho}{\rho_0} g \end{cases} \iff \begin{cases} \frac{\partial p}{\partial r_c} = \rho_0 \left(\frac{u^2}{r_c} + r_c \Omega^2 + 2u\Omega_T \right) \\ \frac{\partial p}{\partial z} = -\rho g \end{cases} \quad (2.12)$$

After computation (see appendix 5.3) it is found that

$$p(r, \theta) = \rho_0 \left(-\frac{\Omega^2 R^2}{4} \left(\frac{R}{r} \right)^4 + \frac{1}{2} r^2 \sin^2 \theta \Omega^2 - 2\Omega\Omega_T R^2 \frac{R}{r} \right) + a(z) \quad (2.13)$$

The influence of the rotating sphere must become negligible for $r \rightarrow +\infty$, it comes from this that $a \equiv 0$. Given that $\frac{\partial p}{\partial z} = -\rho g$, we deduce the expression of ρ :

$$\rho(r, \theta) = \frac{\rho_0}{g} \left(-\Omega^2 R^6 \frac{z}{r^6} - 2\Omega\Omega_T R^3 \frac{z}{r^3} \right) \quad (2.14)$$

2.3 Internal gravity waves

In this section, we study the physical characteristics of internal gravity waves, which are waves forming in a stably stratified fluid [18, 8].

2.3.1 Brunt-Väisälä frequency

In this subsection, we characterise the frequency of internal gravity waves by defining the Brunt-Väisälä frequency.

Definition 2.3.1. The **Brunt-Väisälä** frequency is defined by :

$$N = \sqrt{-\frac{g}{\rho} \frac{\partial \rho}{\partial z}} \quad (2.15)$$

With ρ the fluid density and g the acceleration due to the gravity.

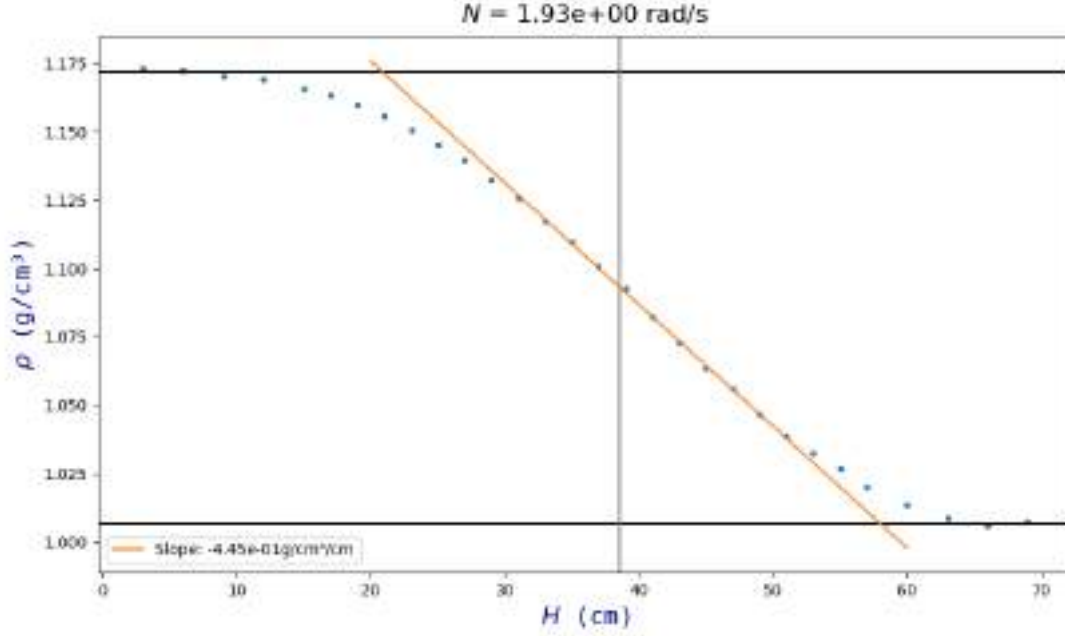


Figure 2.2: Background density profile estimated by experimental sample analysis. The stratification having an age of two months, we note that the initial density profile, linearly stratified only in the middle of the tank, has become smoother at the top and bottom due to salt diffusion

Proposition 2.3.1. The Brunt-Väisälä frequency represents the frequency of a vertical motion oscillation.

Proof. We consider an inviscid fluid in order that a particle would only be exposed to gravity and buoyancy. We isolate a specific particle of volume $dx \cdot dy \cdot dz$, and we move it from a position $z + \delta z$ to its initial and equilibrium altitude z . We note $\rho(z)$ the density of a fluid particle at altitude z . According to Newton's second law of motion, we have :

$$\sum \vec{F} = m\vec{a} \quad (2.16)$$

\hat{z} axis is oriented upwards. Two forces apply to the fluid particle: its weight and buoyancy. We then have:

$$-dx \, dy \, dz \, \rho(z)g\hat{z} + dx \, dy \, dz \, \rho(z + \delta z)g\hat{z} = \sum \vec{F} = dx \, dy \, dz \, \rho(z) \frac{d^2\delta z}{dt^2}$$

Projecting on the \hat{z} axis:

$$\iff \frac{d^2\delta z}{dt^2} \rho(z) = g(\rho(z + \delta z) - \rho(z)) \iff \frac{d^2\delta z}{dt^2} = \frac{\delta z}{\rho(z)} \frac{g(\rho(z + \delta z) - \rho(z))}{\delta z}$$

When δz tends towards zero, the expression becomes:

$$\frac{d^2\delta z}{dt^2} = \delta z \frac{g}{\rho(z)} \frac{\partial \rho}{\partial z} = -N^2 \delta z$$

Which is the equation $\frac{d^2\delta z}{dt^2} + N^2\delta z = 0$ of an harmonic oscillator in the vertical direction. \square

Brunt-Väisälä frequency can be estimated from a density profile, as shown on fig.2.2. We notice that N can be assumed constant, or in other words the fluid is linearly stratified, for an altitude about 30 to 50 cm. The vertical density profile adopted here is introduced in section 3.1.

2.3.2 Properties of internal gravity waves

In this subsection, we consider an internal gravity wave of the form $u = u_0 \exp(i(\omega t - \vec{k} \cdot \vec{r}))$, where \vec{k} is the wave vector, ω the frequency and u_0 wave's amplitude. \vec{k} is forming a θ angle with the vertical axis. We also assume the Brunt-Väisälä frequency N to be constant.

Proposition 2.3.2. The dispersion relation of an internal gravity wave is $\omega^2 = N^2 \cos^2 \theta$, with θ the angle formed between the vertical axis and the $\vec{\delta l}$ vector representing the motion of a fluid particle.

Proof. As done in the previous section, we apply Newton's 2nd law to a fluid particle, but considering now a motion in any direction $\vec{\delta l}$ forming an angle θ with the vertical axis. We have:

$$\rho(z) \frac{d^2 \vec{\delta l}}{dt^2} = -g\rho(z)\hat{z} + g\rho(z + \delta z)\hat{z}$$

Where $\delta z = \vec{\delta l} \cdot \hat{z} = \delta l \cos \theta$. We then introduce the quantity $\delta \rho = \rho(z + \delta z) - \rho(z)$. The previous expression can be rewritten

$$\rho(z) \frac{d^2 \vec{\delta l}}{dt^2} = \delta \rho g \hat{z}$$

As previously, we rewrite this density difference: $\delta \rho = \delta z \frac{\rho(z + \delta z) - \rho(z)}{\delta z} \rightarrow_{\delta z \rightarrow 0} \delta z \frac{d\rho}{dz} = \delta l \cos \theta \frac{d\rho}{dz}$. Coming back to Newton's second law, we get:

$$\rho(z) \frac{d^2 \vec{\delta l}}{dt^2} = \delta l \cos \theta \frac{d\rho}{dz} g \hat{z}$$

We eventually project this expression on $\frac{\vec{\delta l}}{\delta l}$ and notice the Brunt-Väisälä frequency appearance, dividing by ρ both sides of the equation:

$$\frac{d^2 \delta l}{dt^2} = -\delta l N^2 \cos^2 \theta$$

Consequently, we have $\omega^2 = N^2 \cos^2 \theta$. □

Proposition 2.3.3. Group velocity of an internal gravity wave is orthogonal to its phase velocity.

Proof. Group velocity is $\vec{v}_g = \sum_i \frac{\partial \omega}{\partial k_i} \vec{e}_i$ and phase velocity is $\vec{v}_\varphi = \frac{\omega}{k} \frac{\vec{k}}{k}$.

In order to simplify, we choose a basis such that the \vec{k} vector is in the plane xOz , reducing to a 2D problem. As previously, θ denotes the angle between \hat{z} axis and \vec{k} . We then obtain:

$$\vec{v}_g \cdot \vec{v}_\varphi = \frac{\omega k_i}{k^2} \frac{\partial \omega}{\partial k_i} = \frac{1}{2} \frac{k_i}{k^2} \frac{\partial \omega^2}{\partial k_i} = \frac{1}{2} \frac{k_i}{k^2} \frac{\partial N^2 \frac{k_z^2}{k_z^2 + k_x^2}}{\partial k_i}$$

given that $\cos \theta = \frac{k_z}{\sqrt{k_x^2 + k_z^2}}$.

For $k_i = k_x$,

$$\frac{1}{2} \frac{k_x}{k^2} \frac{\partial N^2 \frac{k_z^2}{k_z^2 + k_x^2}}{\partial k_x} = -\frac{k_x^2 k_z^2}{k^6} N^2$$

For $k_i = k_z$,

$$\frac{1}{2} \frac{k_z}{k^2} \frac{\partial N^2 \frac{k_z^2}{k_z^2 + k_x^2}}{\partial k_z} = \frac{k_x^2 k_z^2}{k^6} N^2$$

Consequently, summing on k_x and k_z , we get that:

$$\vec{v}_g \cdot \vec{v}_\varphi = \frac{\omega k_x}{k^2} \frac{\partial \omega}{\partial k_x} + \frac{\omega k_z}{k^2} \frac{\partial \omega}{\partial k_z} = \frac{k_x^2 k_z^2}{k^6} N^2 - \frac{k_x^2 k_z^2}{k^6} N^2 = 0$$

So group velocity is orthogonal to phase velocity. □

2.4 Instabilities

Internal gravity waves are a simple example of waves added to a base flow that can help generating instabilities. There are other kinds of instabilities in stratified shear flows and we will introduce some of them in this section.

As mentioned in [19], ellipsoids rotating in stratified fluids generate various types of instabilities.

These instabilities can be, in a first approach, decomposed in a periodic function similar to $\exp(i(\omega t - \vec{k} \cdot \vec{r}))$ and put into linearised Navier-Stokes equation to study their behaviour, numerically or analytically, performing linear stability analysis.

2.4.1 Centrifugal instabilities

Centrifugal instabilities are caused by an unstable equilibrium between centrifugal force and radial pressure gradient [2]. The Rayleigh criterion is a necessary and sufficient condition for the centrifugal instability [2]. Centrifugal instability is expected when the following equation is verified [2, 19]:

$$\phi = \frac{1}{r^3} \frac{\partial(r^2 \Omega)^2}{\partial r} \Big|_{\rho} < 0 \quad (2.17)$$

Where ϕ is the Rayleigh discriminant.

In other words, a centrifugal instability happens if ϕ decreases with the radius along isopycnal surfaces, namely surfaces of constant density.

2.4.2 Double-diffusive and viscous-diffusive instabilities

Double-diffusive instability occurs when two different gradients are acting on density. For instance, let's consider a tank filled with water such that water at the top is saltier than water at the bottom, and the same for temperature. If we now look at a fluid particle pushed upwards, its properties will interact with the ones in its new position. However, properties are not modified at the same velocity given that diffusion coefficients for salt (κ_s) and temperature (κ_T) verify $\kappa_s \ll \kappa_T$. So particle's temperature will grow quicker than particle's salinity. Its density will then decrease as hot water is less dense than cold water. Consequently, the particle will rise until it reaches to the top of the tank. This situation is thereby unstable as a small perturbation conducts to a significantly different state. On the contrary, if water at the bottom is saltier, a shifted particle will tend towards its initial position.

The same idea can be applied to density and velocity fields.

A similar mechanism is involved for viscous-diffusive instability, also referred as McIntyre instability [10]. McIntyre criterion generalises Rayleigh criterion for both centrifugal and viscous-diffusive instabilities. Threshold for instability's appearance is expressed [9, 10]:

$$\frac{\tan \Theta}{\tan \Gamma} < \frac{\text{Sc}}{4} \left(1 + \frac{1}{\text{Sc}} \right)^2 \quad (2.18)$$

Where Θ is the angle between isopycnals and the vertical, Γ the angle between the lines of constant circulation and the vertical, and $\text{Sc} = \frac{\nu}{\kappa}$ is the Schmidt number.

2.4.3 Convective instability

Convective instability mechanism is intuitive: under the gravity effect, denser fluid sinks and lighter fluid rises. This mechanism is for instance present for a boiling water stove.

Having these instabilities criteria coupled to the equations of the base flow can then lead to a numerical investigation to determine the mechanisms responsible for the instabilities observed around the rotating sphere.

Chapter 3

Experimental work

In this chapter, we present the experiments conducted during the internship. The main goal is to check the accordance between theory, numerical results and experiments. To do so, some experiments have been carried out. All of them are more or less linked with a common method to measure fluid's velocity field: particle image velocimetry (PIV), introduced in section 3.2. In the very first experiment, a method to create an uniform stratification has been used in order to check PIV particles' efficiency. Then, a velocity field settling measurement has been performed without and with tank rotation. After this, instabilities have been measured without tank rotation. Because of a lack of time caused by some technical issues, instabilities could not be measured with a rotating tank.

3.1 Experimental setup

During this training, the experimental setup, shown in fig. 3.1, is composed of a cylindrical tank of 1 m in diameter and 1.6 m high. This tank is filled with salt water in order to create a salt concentration gradient, with fresh water at the top and very salty water at the bottom. Stratification is depicted on fig. 2.2. Water was initially not stratified below and above on about twenty centimeters, but due to salt diffusion, the density profile became smoother. Under the tank is put a rotating table able to set all the apparatus until a 1 Hz rotation. The meddy is embodied by a solid spheroid placed on a vertical rotating axis. It can be put in rotation independently of the table rotation. In order to measure fluid particles' velocity (see next section), reflecting particles having the appropriate density are injected in the equatorial plane of the meddy. A laser placed next to the tank can then light up this zone with a planar shape.

3.2 Particle Image Velocimetry

Particle Image Velocimetry (referred as PIV thereafter) is a non pervasive way to measure velocity flow in a fluid. It consists in adding reflective hollow particles to the fluid, which will then be lightened by a laser sheet in order to check their motion through the time with a camera. These particles are conceived to have the same density as the fluid and consequently follow correctly the flow.

To estimate motions in the fluid, during this internship, the Python library `dpivsoft` has been used. The program decomposes a given image in boxes of chosen length (typically, 32 or 64 pixels), and performs a cross-correlation between this image and the following to calculate box's movement. There are consequently several parameters to fit: box size, frame acquisition rate, sensitivity etc.

3.3 Experiment zero: stratification elaboration with the double-bucket method

Experimentally speaking, particle quantity must be well adjusted; too much particles impedes measurements whereas too little particles can let zones with no velocity information. It is moreover frequently necessary to add particles since they seem to sediment quickly. However, particles' density specified by the manufacturer



Figure 3.1: Experimental setup. The water is 70 cm high, saline at the bottom, fresh at the top and stratified around the sphere. The sphere is visible along the vertical rotating black axis. An embedded camera allows to do PIV in the tank's frame of reference.

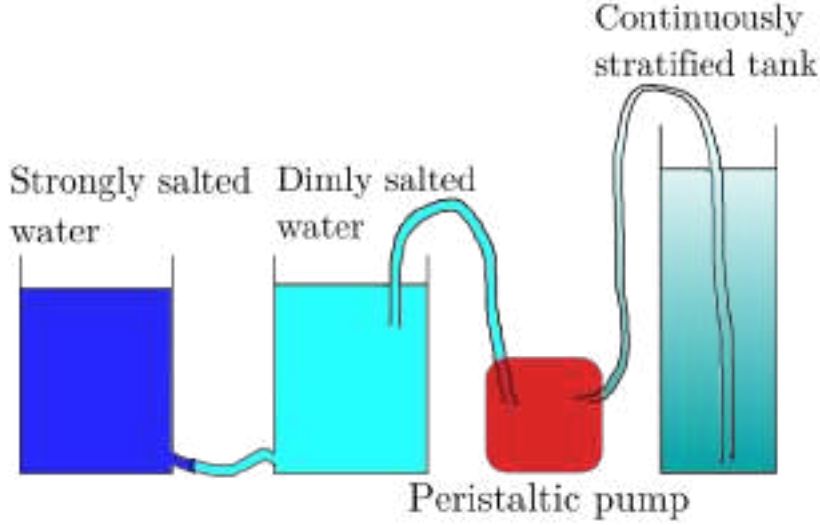


Figure 3.2: Double-bucket system setup

being between 1.05 and 1.15 ¹, this apparent sedimentation was quite surprising. We thus decided to check particles' efficient density by putting a large amount of them in a stratified fluid.

To make a stratification, we used the double-bucket method, presented in fig. 3.2. It consists in filling two buckets, one with fresh water and the other with strongly salty water, and connect them via their bottom. Then, water is sucked up from the fresh water bucket thanks to a pump, and discharged in the recipient in which we want to make a stratification, with a pipe going through to the bottom.

We used fresh water and saline water with a density around 1.14 to fill the two buckets. The pump involved was a peristaltic one, which allowed to adjust the flow in order not to disturb the stratification with a too rapid water addition in the graduated cylinder. After particles' addition, we noticed that even if particles' density was normally higher than 1.05, some particles stayed at the surface of the stratification, namely where there should only be fresh water. Many of them also sank to the recipient's bottom. In spite of this, enough particles were positioned on the whole graduated cylinder. It was consequently possible to get samples of particles having the wished density, depending on the observed zone, as water at the sphere's equator altitude is denser than water at the upper pole.

3.4 First experiment: velocity settling

3.4.1 Experiment 1: velocity settling without tank rotation

Presentation

The base flow has been computed in the previous chapter. Its setting up can then be studied.

In order to do PIV, hollow PIV particles must be disposed all over the target zone as explained previously. However, at the starting, the fluid in the tank does not move so it is not possible to make use of the base flow to mix PIV particles in the fluid. This point was quite problematic since it is hard for the experimenter to mix PIV particles by himself. It was therefore necessary to add PIV particles in sufficient quantity before the end of the previous experiment.

The main mechanism for velocity transmission is assumed to be diffusion. Stratification indeed inhibits motions induced by forces with vertical components like weight and buoyancy.

Navier-Stokes equation is thereby reduced to the following diffusion equation:

$$\partial_t \vec{u} = \nu \vec{\Delta} \vec{u} \quad (3.1)$$

¹Manufacturer's information on hollow PIV particles

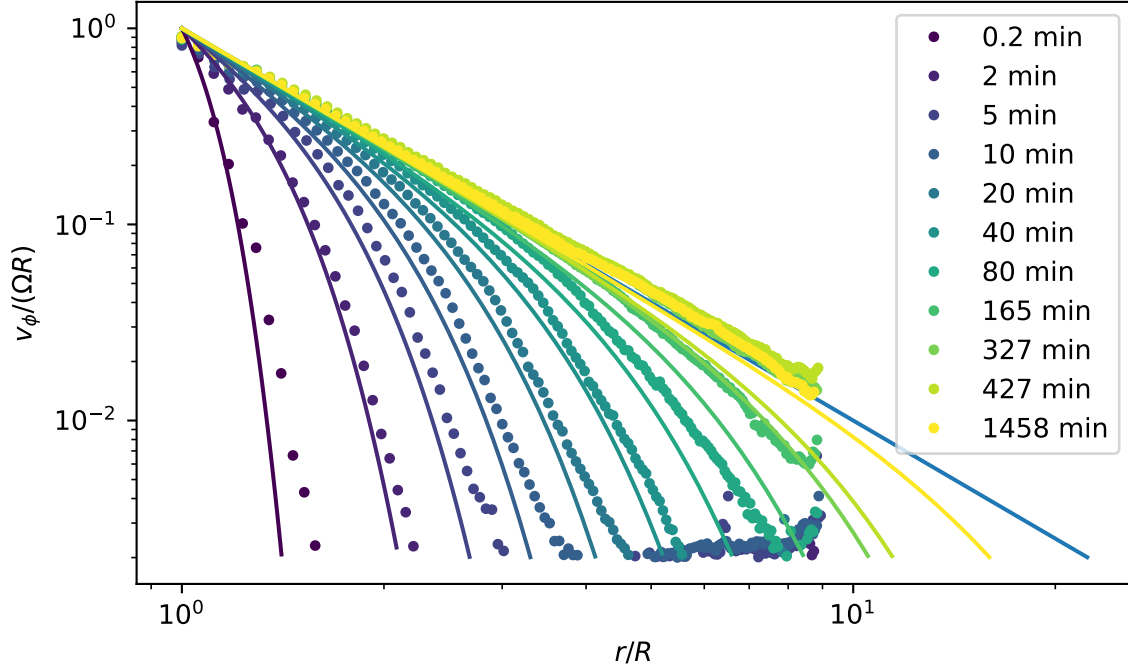


Figure 3.3: Velocity settling measurement: lines correspond to theoretical expected velocity whereas dots represent the experimental measured velocity. Theoretical velocity is obtained by numerical solving of eq. (3.1) by the spectral solver Dedalus (see appendix 5.4)

Considering only orders of magnitude, this diffusion equation becomes $\frac{u}{\Delta t} = \nu \frac{u}{L^2}$ where Δt and L are respectively a characteristic time and a characteristic length of the system. This is equivalent to $\Delta t = \frac{L^2}{\nu}$. Taking now as characteristic length the distance to the sphere, we are able to estimate the time needed for the velocity settling. For instance, a particle placed 6 radius away from the sphere will require $\frac{(6R)^2}{\nu} = 57\,600\text{ s} = 16\text{ h}$ to be set into motion. This coarse estimation can be improved by solving the diffusion equation (3.1) thanks to the spectral solver Dedalus, as shown on fig. 3.3.

Results and discussions

The results, depicted on fig. 3.3, show that experimental velocity is quicker than theoretical. This conclusion is quite surprising since stratification impedes vertical motion and thus drastically inhibits all mechanisms directed upwards and downwards like convection, that could play a role in the velocity settling.

3.4.2 Experiment 2: measurement of the velocity settling with a rotating tank

Presentation

The target is to do again the experiment presented in a previous section within a rotating frame. We expected to obtain the same results as before once reached solid-body rotation for the fluid, because in the reference frame of the fluid, the situation is identical.

Results and discussions

The main problem here has been the delay for solid rotation setting up in the fluid. It took roughly 24 h to go back to an immobile state for particles seen by the on-board camera. This delay has been quite problematic because of the sedimentation of PIV particles. It has been necessary to add particles while the table was rotating in order to get usable data. Similarly to the immobile experiment on velocity settling, the measured velocity was significantly too high.

3.5 Instabilities study

3.5.1 Dimensionless numbers

Dimensionless numbers are useful in fluid mechanics as they help quantifying how much is a phenomenon important regarding to another. For instance, Reynolds number depicts the ratio between convection and diffusion, and then indicates if the fluid properties are more transported by convection or molecular diffusion, which are different mechanisms. Knowing this could lead to simplifications in the equations in a warranted way.

Definition 3.5.1. Reynolds number, referred as Re , is defined by $Re = \frac{v_{ref} L_{ref}}{\nu}$, where v_{ref} is the average velocity, L_{ref} a reference length and ν the kinematic viscosity of the fluid, in other words the dynamic viscosity divided by the fluid density. Given that a typical velocity is $R\Omega$, where Ω is the angular velocity of the sphere, and a characteristic length is R , this expression can be rewritten $Re = \frac{R^2 \Omega}{\nu}$.

For seawater, $\nu \simeq 1 \times 10^{-6} \text{ m}^2 \text{ s}^{-1}$, $R = 4 \text{ cm}$, and Ω can be set to 0.5 rad s^{-1} for this example. So $Re = \frac{(4 \cdot 10^{-2})^2 \times 0.5}{1 \cdot 10^{-6}} = 800$.

Another dimensionless number that will be used is the Froude number.

Definition 3.5.2. Froude number, as for it, characterises the ratio between gravitational and inertial forces. It has several definitions, which are not all consistent between them [4]. The chosen one links Froude number to Brunt-Väisälä frequency as $Fr = \frac{\Omega}{N}$.

During the internship, a measurement of N in the experimental stratification conducted to $N = 1.93 \text{ rad s}^{-1}$ (see fig. 2.2). A typical angular velocity for the rotating sphere is 0.5 rad s^{-1} . So $Fr = \frac{\Omega}{N} = 0.26$.

These two numbers will help in the next section, in which we will present an experimental and numerical instability criterion for a rotating sphere based on Re and Fr .

To quantify the importance of centrifugal force regarding to Coriolis force, Rossby number will be used.

Definition 3.5.3. Rossby number, denoted as Ro , is defined by $Ro = \frac{v_{ref}}{L_{ref} f} = \Omega f$, where $f = 2\Omega_T$ is the Coriolis parameter.

Consequently, neglecting Coriolis force is equivalent to set Ro to $+\infty$. This case corresponds to a non rotating tank.

Definition 3.5.4. Ekman number, referred as Ek , describes the ratio between viscous and Coriolis forces, and is defined by $Ek = \frac{\nu}{\Omega_T H^2}$, where H is the water's height in the tank.

Ekman number is used in order to get an estimation of the needed time for obtaining a solid rotation for the liquid when putting the tank in rotation. This spin-up time scale is, according to [14, 17], mainly caused by diffusion, so equal to $\mathcal{O}(Ek^{-1} \Omega_T^{-1}) = \mathcal{O}(\frac{H^2}{\nu})$.

In non stratified fluids, a phenomenon named Ekman pumping contributes to accelerate this spin-up time. Indeed, at the tank's bottom, fluid particles put into a rotating motion are subject to centrifugal force and consequently deviated outwards. This creates convection in the fluid that speeds up the solid rotation setting up.

However, in our case, the tank is not fully homogeneous as layers close to the sphere are stratified. It is consequently hard to evaluate the impact of this mechanism in the needed time for obtaining a solid rotation. Ekman pumping may happen for the homogeneous zones at the top and bottom, and consequently accelerates the spin up, but this is hard to quantify.

Definition 3.5.5. Schmidt number is a dimensionless number corresponding to the ratio of kinematic viscosity and density diffusivity. Thus it is expressed as $Sc = \frac{\nu}{\kappa}$.

Schmidt number is a good indicator to know if density diffusivity can be neglected regarding to kinematic viscosity and vice versa. For instance, salt density diffusion coefficient κ_s is really low, approximately $\kappa_s \simeq 1 \times 10^{-9} \text{ m}^2 \text{ s}^{-1}$ whereas κ_T the thermal diffusivity is around $\kappa_T \simeq 1 \times 10^{-7} \text{ m}^2 \text{ s}^{-1}$. As said before, kinematic viscosity for saline water is about $1 \times 10^{-6} \text{ m}^2 \text{ s}^{-1}$. Thus, salt diffusion can be neglected regarding to kinematic viscosity, but that is not the case for thermal diffusivity.

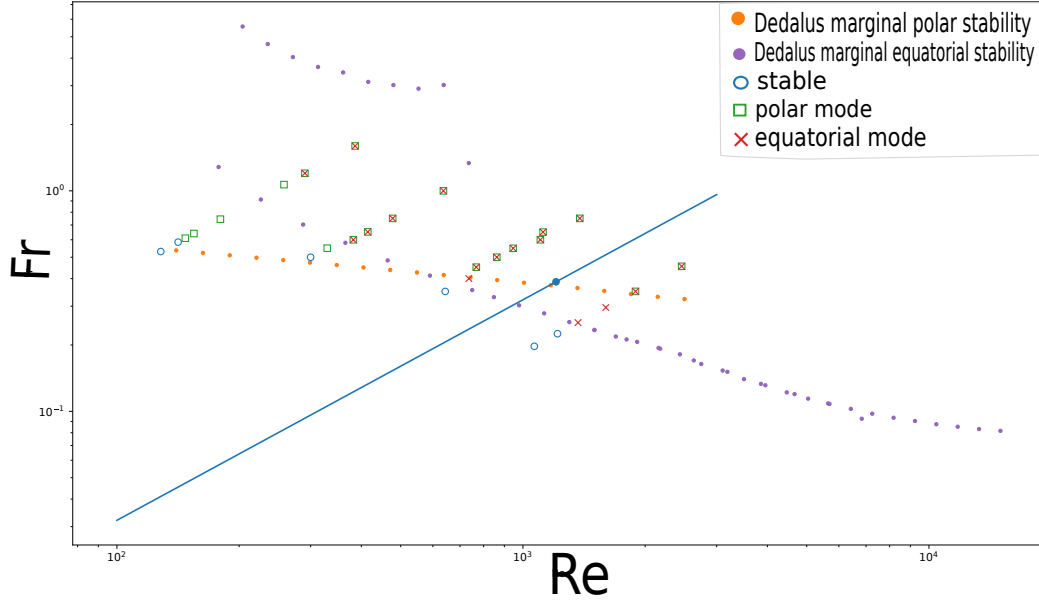


Figure 3.4: Stability diagram previously obtained thanks to numerical and experimental studies

3.5.2 Criteria for meddies' instability beginning

Previous unpublished work done in 2014 by IRPHÉ researchers Patrice MEUNIER and Benjamin MIQUEL set up that instabilities at the poles and at the equator follow two distinct tendencies indicated by two straight lines in the parameter space of Reynolds and Froude numbers, as shown on fig 3.4.

Different behaviours are then expected depending on the values of Re and Fr numbers. However, setting up a tank with stratified water layers is time-consuming. A strategic approach to easily observe different types of instabilities with accessible laboratory equipment is to choose appropriate values of R , N and ν .

For this training, all experiments are thus placed on the blue line, with $N \simeq 2$, $R = 4\text{ cm}$ and $\nu = 1 \times 10^{-6}\text{ m}^2\text{ s}^{-1}$. This configuration allows to observe equatorial instabilities alone, and both polar and equatorial instabilities with a higher Ω , but this is not possible to only have a polar instability.

3.5.3 Second experiment: measurement of instabilities in the flow without tank rotation

Presentation

The aim of this experiment is to study the formation of instabilities at the equator and at the poles. We consequently rise the sphere's angular velocity to a level at which we expect to observe instabilities. Since the experimental setup only allows to get information in one horizontal plane, it is not possible to do simultaneously measurements at the equator and at the poles. It is consequently required to perform at least two times this experiment.

The first experiment was dedicated to flow instabilities at the equator, with an angular velocity of $\Omega = 2\pi \times 0.05\text{ rad s}^{-1}$, which brings the system in a zone of equatorial instabilities but no polar ones according to fig 3.4. With an angular velocity about $2\pi \times 0.1\text{ rad s}^{-1}$, we get instabilities similar to those on fig 1.2.

By rising angular velocity to $2\pi \times 0.12\text{ rad s}^{-1}$, instabilities also appear at the poles, as expected. Sphere's projection is shown on fig 3.5 and shadowgraphy method reveals the instability patterns.

Results and discussions

Qualitatively, the polar instability seems usually stronger at the bottom than at the top (this is not visible on fig 3.5). This may be caused by the free surface above the sphere.

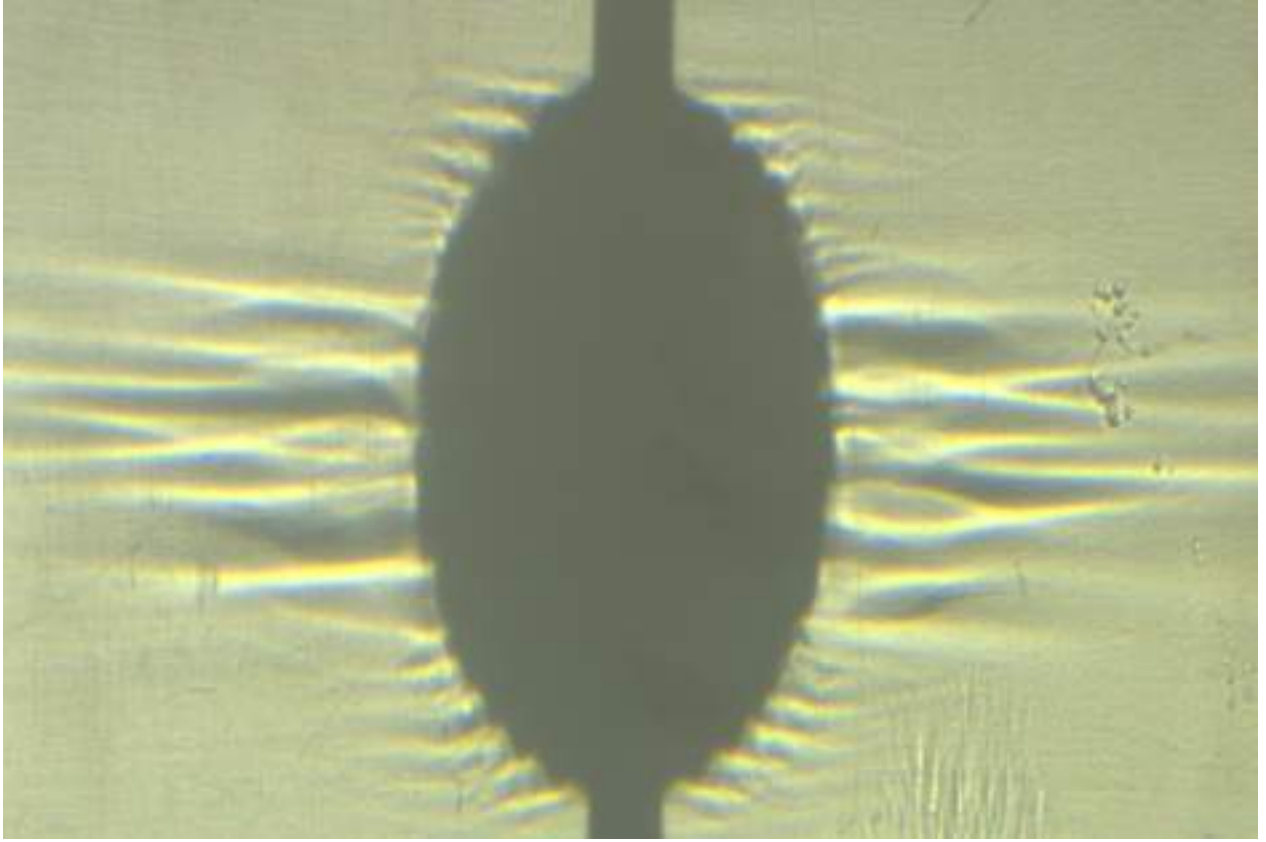


Figure 3.5: Instabilities at the equator and at the poles. Obtained by shadowgraphy, in the same way as 1.2

It has been assumed that the instability has a structure in $\exp(imt)$. By performing a Fourier transform of the velocity field, we are able to extract information on its frequency.

To evaluate instabilities' impact, we focused on radial velocity rather than tangential velocity because the latter has already a strong component due to the base flow whereas the former should be only caused by perturbations. Results are shown on fig. 3.6, which depicts the observation window of the camera at a fixed time. The solid sphere is located at position (0; 0) and PIV particles' radial velocity is indicated by the color map.

A filtering of the instability has been performed on the second picture, by doing a fast Fourier transform with the `numpy` library. The circular rays presents on the filtered PIV are not caused by a physical phenomenon but by a PIV program bias, which tends to round pixels' moving value to an int, creating a peak locking effect.

Fig. 3.6 indicates that the equatorial instability has an azimuthal wave number $m = 1$ as we are only able to observe one period on the whole sphere's contour. This instability rotates with time so it is possible to estimate its period. In order to, we plotted across time a mean of pixels' value in a fixed square of the picture, using a `numpy` mask to select a zone on all pictures. The result is represented on fig. 3.7.

Using fig. 3.7 to calculate instability's period, by doing a mean on 4 periods, we obtained a period of 38 s.

Instabilities' observation at the upper pole has not been conclusive: light coming from the solid sphere interfered with the weak PIV particles information. Results were consequently noisy and unusable. We also tried to observe in the vicinity of the 45° latitude, but here also, the signal was perturbed.

3.6 General results and discussions

In this chapter, we conducted experiments with the experimental setup presented in fig. 3.1, involving the Particle Image Velocimetry method to estimate fluid velocity.

We first attempted to check if the main mechanism for the velocity settling was molecular diffusion, as it should be in a stratified fluid with a shear flow. We tried to measure it without and with table rotation.

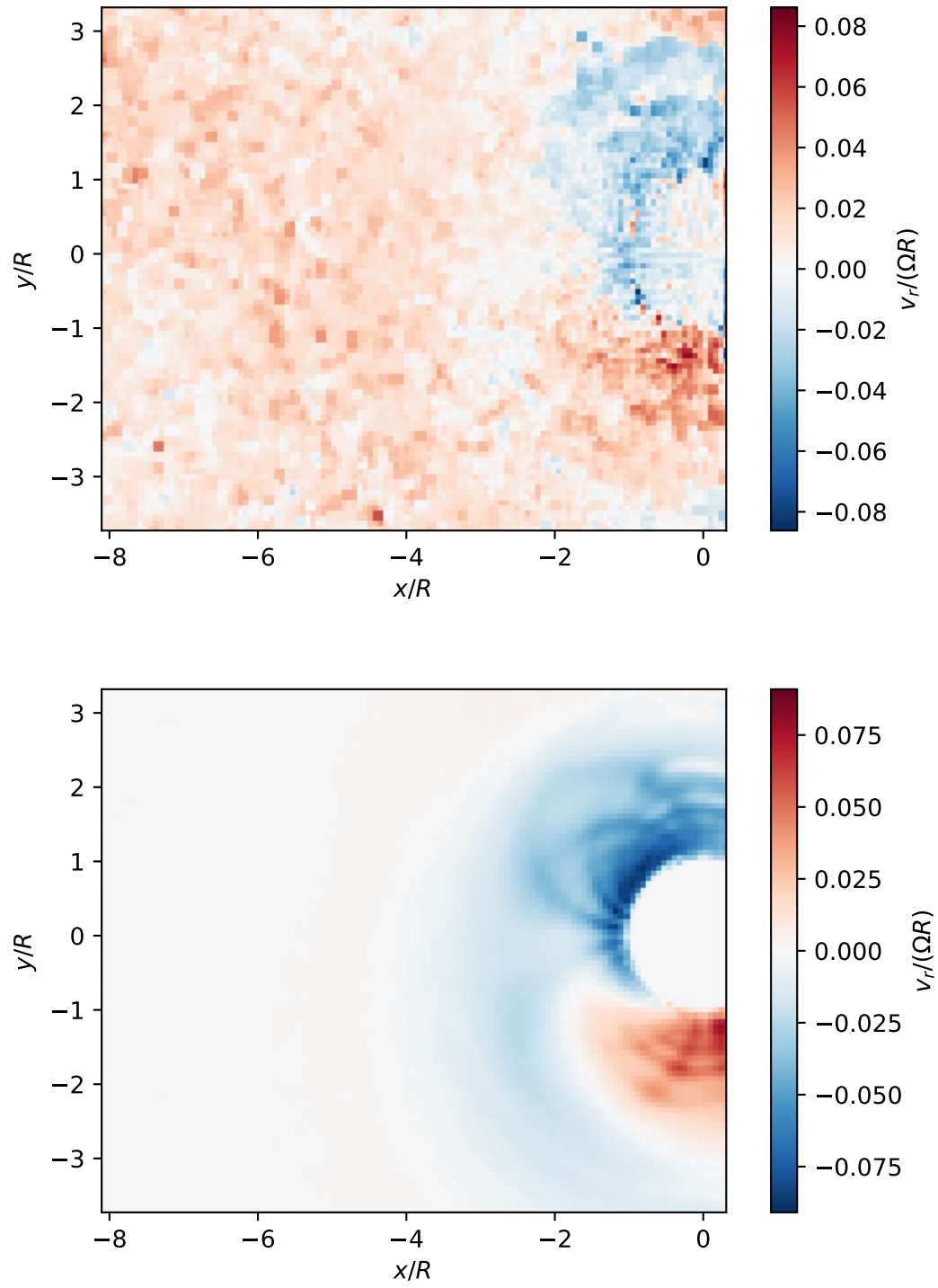


Figure 3.6: Raw PIV results and filtered PIV results on radial velocity at the equator.

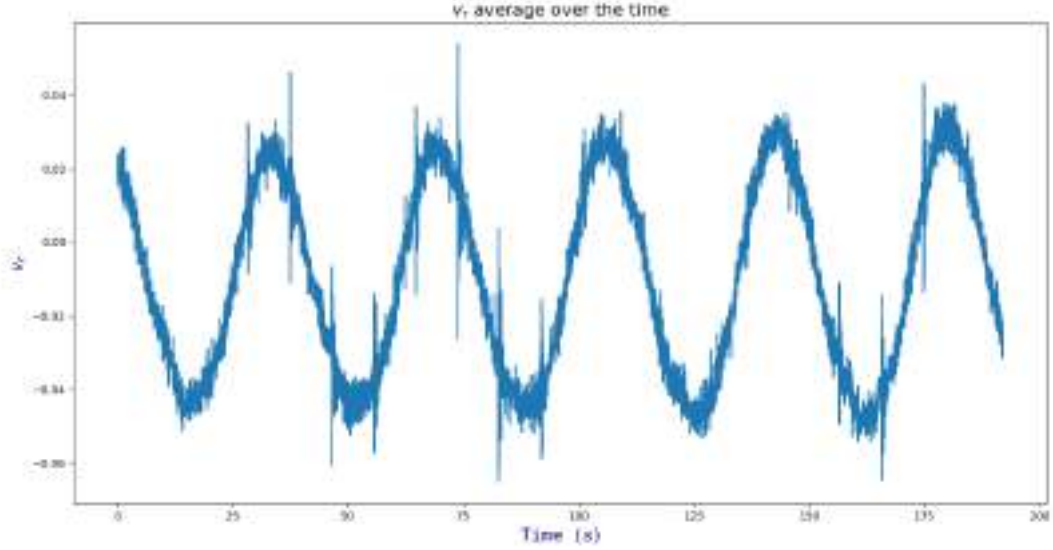


Figure 3.7: Radial velocity plotted over the time

The settling velocity was too high in both experiments, pointing out that the Stokes model does not fully describe it.

After that, we focused on instabilities, and introduced a stability criterion for polar and equatorial instabilities derived from previous works at the laboratory. This criterion has been well confirmed by all the performed experiments. We then observed the equatorial instability thanks to PIV. Even with no filtering, we obtained significant results, available on fig. 3.6, that reached to the identification of a normal mode $m = 1$ for this instability. Its period could be estimated to 38 s. Polar instability could not be resolved due to noisy measurements.

Chapter 4

Conclusion

During this internship, we explored both theoretically and experimentally the instabilities generated by a rotating spheroid placed in stratified salt water. This setup attempts to model the interaction of a meddy, a hot and salty water eddy, with the adjacent Atlantic Ocean. Understanding the effects of meddies may help to improve knowledge on both oceanic mixing and thermohaline circulation, in particular the Atlantic Meridional Overturning Circulation (AMOC) which had hit the headlines these last months [5]. After introducing the concept of stratification, we solved equations for the base flow generated by a rotating sphere in a continuously stratified fluid for velocity, pressure and density. We then studied different types of instabilities in stratified fluids, such as internal gravity waves, and demonstrated some properties of the latter.

Afterwards, we performed experiments to check the accordance between theory and reality, and that reached to a misunderstanding of the velocity settling, with an experimental measurement higher than expected. A lack of time prevented further investigations. Some conceivable hypotheses would be a bias in the PIV particles submitting them to a bigger centrifugal force than the rest of the fluid or an irrelevant removal of a mechanism. A numerical solving of a more complete equation than eq. (3.1) could help to estimate the contributions related to each phenomenon. Regarding instabilities, experiments without rotating table have revealed the presence of a normal mode of 1, and all experiments were in accordance with the previous results depicted on fig. 3.4, consolidating this stability criterion.

To go further, it could be interesting to change meddy's shape in oblate or prolate ones. For instance, given that previous studies [19] have investigated on instabilities generated by a rotating cylinder, adopting a prolate shape could reach to a behaviour more similar to a cylinder. And due to stratification, meddies in the oceans tend towards an oblate shape.

About instabilities, an extension of the training would be to find out if there are other normal modes hidden behind the one studied. Another track could be to look for instabilities in the vertical plane instead of horizontal one, as performed in this training. However, this would require a camera to be installed either outside the tank, where it could be disturbed by the thickness and curvature of the Plexiglas, or inside the tank, where it would have to be perfectly sealed.

Eventually, meddies are composed by water hotter than Atlantic seawater, so it could be also relevant to check the influence of heating on perturbations.

Chapter 5

Appendix

5.1 Organisation chart

In this section, the organisation chart of the laboratory is provided.

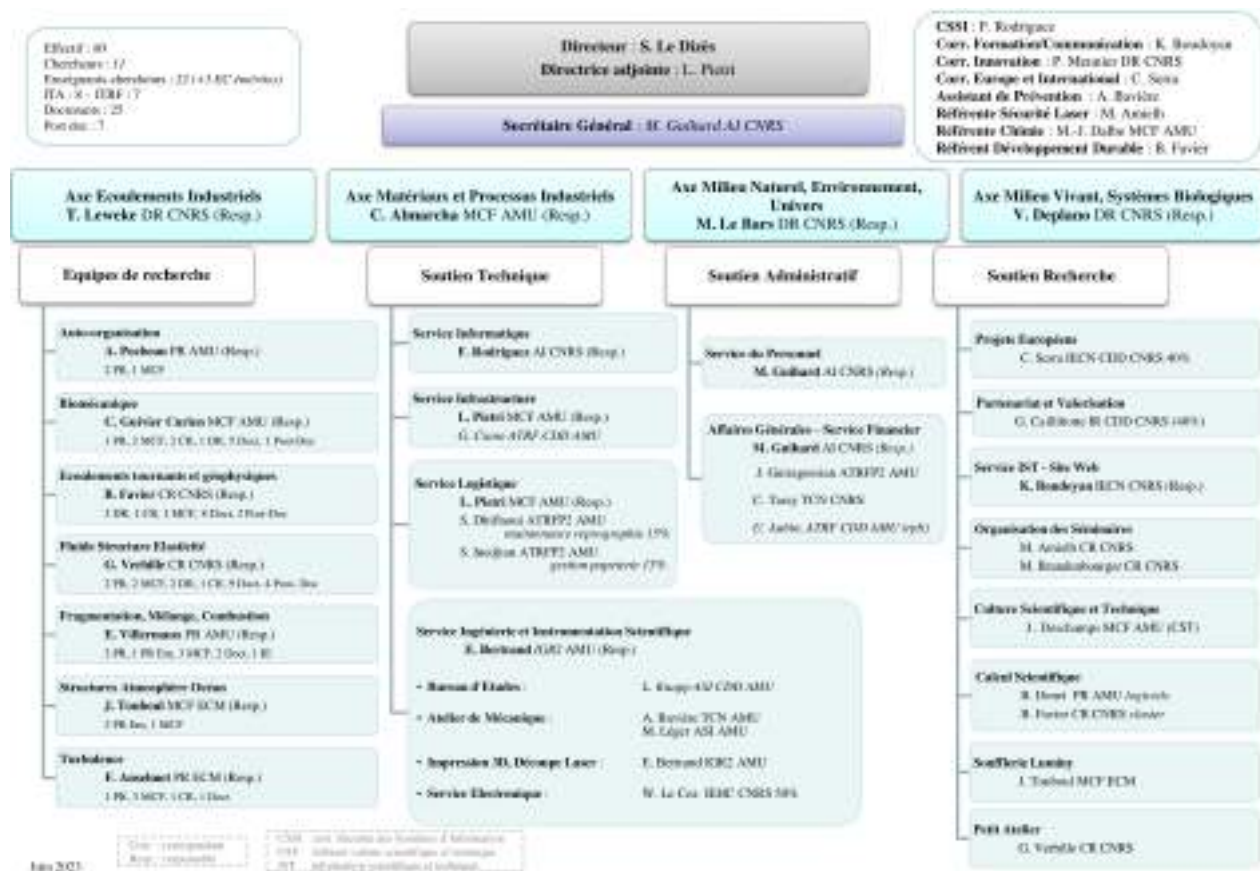


Figure 5.1: Organisation chart of the laboratory

5.2 Nomenclature

\hat{z}	Unit vector $\frac{\vec{z}}{\ \vec{z}\ }$
Ω	Sphere's angular speed (rad s^{-1})
Ω_T	Earth's angular speed (rad s^{-1})
ρ	Density (kg m^{-3})
κ_S	Salt density diffusion coefficient ($\text{m}^2 \text{s}^{-1}$)
κ_T	Temperature density diffusion coefficient ($\text{m}^2 \text{s}^{-1}$)
Re	Reynolds number
Fr	Froude number
Sc	Schmidt number
Ek	Ekman number
Ro	Rossby number

Table 5.1: Adopted nomenclature

5.3 Detailed calculation of p

In this section, we expose the detailed calculation of the pressure base flow.

We remind here the expression of the Navier-Stokes equation projected on $\vec{e}_{r,c}$ and \vec{e}_z :

$$\begin{cases} -\frac{u^2}{r_c} = -\frac{1}{\rho_0} \frac{\partial p}{\partial r_c} + r_c \Omega^2 + 2u\Omega_T \\ 0 = -\frac{1}{\rho_0} \frac{\partial p}{\partial z} - \frac{\rho}{\rho_0} g \end{cases} \iff \begin{cases} \frac{\partial p}{\partial r_c} = \rho_0 \left(\frac{u^2}{r_c} + r_c \Omega^2 + 2u\Omega_T \right) \\ \frac{\partial p}{\partial z} = -\rho g \end{cases} \quad (5.1)$$

We recognize that the second line of the system is the hydrostatic equation. This will be used after p computation for calculating ρ . To estimate p we must integrate the first equation on r_c . We have from previous computation that $u = \Omega R \sin \theta \left(\frac{R}{r} \right)^2$. Then, we have $r = \sqrt{r_c^2 + z^2}$ from Pythagoras' theorem. We also have the relation $r_c = r \sin \theta$.

Thus,

$$\frac{u^2}{r_c} = \Omega^2 \sin^2 \theta R^2 \left(\frac{R}{r} \right)^4 \frac{1}{r_c} = \Omega^2 \sin^2 \theta R^6 \frac{1}{r^4} \frac{1}{r \sin \theta} = \Omega^2 \sin \theta R^6 \frac{1}{r^5}$$

Multiplying by $1 = \frac{r_c}{r \sin \theta}$, it leads to

$$\frac{u^2}{r_c} = \Omega^2 R^6 \frac{r_c}{r^6} = \Omega^2 R^6 \frac{r_c}{(r_c^2 + z^2)^3}$$

Similarly, for the last term of equation (5.1), we have

$$2u\Omega_T = 2\Omega\Omega_T R^3 \sin \theta \frac{1}{r^2} = 2\Omega\Omega_T R^3 \sin \theta \frac{1}{r^2} \frac{r_c}{r \sin \theta} = 2\Omega\Omega_T R^3 \frac{r_c}{(r_c^2 + z^2)^{3/2}}$$

Replacing in the equation, we get:

$$\frac{\partial p}{\partial r_c} = \rho_0 \left(\Omega^2 R^6 \frac{r_c}{(r_c^2 + z^2)^3} + r_c \Omega^2 + 2\Omega\Omega_T R^3 \frac{r_c}{(r_c^2 + z^2)^{3/2}} \right) \quad (5.2)$$

Noting that

$$\frac{\partial}{\partial r_c} \frac{1}{(r_c^2 + z^2)^2} = -\frac{2(r_c^2 + z^2) \cdot 2r_c}{(r_c^2 + z^2)^4} = -\frac{4r_c}{(r_c^2 + z^2)^3}$$

the first term can be easily integrated. And noticing that

$$\frac{\partial}{\partial r_c} \frac{1}{\sqrt{r_c^2 + z^2}} = -\frac{r_c}{(r_c^2 + z^2)^{3/2}}$$

the same happens for the last term.



Figure 5.2: Example of camera picture

Consequently, it is obtained after integration:

$$\begin{aligned}
 p &= \rho_0 \left(-\frac{\Omega^2 R^6}{4} \frac{1}{(r_c^2 + z^2)^2} + \frac{1}{2} r_c^2 \Omega^2 - 2\Omega\Omega_T R^3 \frac{1}{\sqrt{r_c^2 + z^2}} \right) + a(z) \\
 \Leftrightarrow p(r, \theta) &= \rho_0 \left(-\frac{\Omega^2 R^2}{4} \left(\frac{R}{r} \right)^4 + \frac{1}{2} r^2 \sin^2 \theta \Omega^2 - 2\Omega\Omega_T R^2 \frac{R}{r} \right) + a(z)
 \end{aligned} \tag{5.3}$$

The $z \mapsto a(z)$ is then eliminated as detailed in the report section 2.2.3 by making $r \rightarrow +\infty$.

5.4 Dedalus solver: spectral method for numerical simulations

Dedalus is an open-source and parallelised partial differential equations solver using spectral methods [3]. It is used as a library in Python programs: plain-text strings representing partial differential equations are solved.

Spectral methods expand functions over a set of basis functions in order to discretize them. The obtained series of terms are truncated at the desired mode order N . Remaining coefficients of the sum are then computed thanks to quadrature rules [3].

To solve equations with spectral methods, algebraic equations for the coefficients of the truncated solution are computed, some ways to perform this conversion are the collocation, Galerkin and tau methods, introduced with more details in [3].

5.5 PIV examples

In this section, we introduce the post-processing stage with example pictures. On fig. 5.2 is shown the raw picture from the camera.

To obtain a better velocity estimation near the sphere, we artificially add an image of solid sphere rotating on the zone filled by the meddy. We proceed in the same way for all pictures taken, making the artificial circle rotating at the expected velocity.

We then perform the PIV with the Python library `dpivsoft` [1].



Figure 5.3: The previous picture (fig. [5.2](#)) with a synthetic solid rotation added

List of Figures

1.1	An overview of meddies	1
1.2	Instabilities at the sphere's equator. Obtained by shadowgraphy, a technique which consists here in projecting the enlightened sphere on a white screen. Light is deviated depending on the refractive index of the water, which varies with density.	2
2.1	Velocity field obtained in equation (2.11): top view (2.1a) and side view (2.1b)	6
2.2	Background density profile estimated by experimental sample analysis. The stratification having an age of two months, we note that the initial density profile, linearly stratified only in the middle of the tank, has become smoother at the top and bottom due to salt diffusion	7
3.1	Experimental setup. The water is 70 cm high, saline at the bottom, fresh at the top and stratified around the sphere. The sphere is visible along the vertical rotating black axis. An embedded camera allows to do PIV in the tank's frame of reference.	11
3.2	Double-bucket system setup	12
3.3	Velocity settling measurement: lines correspond to theoretical expected velocity whereas dots represent the experimental measured velocity. Theoretical velocity is obtained by numerical solving of eq. (3.1) by the spectral solver Dedalus (see appendix 5.4)	13
3.4	Stability diagram previously obtained thanks to numerical and experimental studies	15
3.5	Instabilities at the equator and at the poles. Obtained by shadowgraphy, in the same way as 1.2	16
3.6	Raw PIV results and filtered PIV results on radial velocity at the equator.	17
3.7	Radial velocity plotted over the time	18
5.1	Organisation chart of the laboratory	20
5.2	Example of camera picture	22
5.3	The previous picture (fig. 5.2) with a synthetic solid rotation added	23

Bibliography

- [1] J. A.-C. al. “DPIVSoft-OpenCL: A multicore CPU–GPU accelerated open-source code for 2D Particle Image Velocimetry”. 2022. URL: <https://www.softxjournal.com/action/showPdf?pii=S2352-7110%2822%2900174-1>.
- [2] P. Billant and F. Gallaire. “Generalized Rayleigh criterion for non-axisymmetric centrifugal instabilities”. 2005. P. 365. URL: http://www.journals.cambridge.org/abstract_S0022112005006464.
- [3] K. J. Burns et al. “Dedalus: A flexible framework for numerical simulations with spectral methods”. 2020. American Physical Society (APS). URL: <http://dx.doi.org/10.1103/PhysRevResearch.2.023068>.
- [4] *Definition of the Froude number, American Meteorological Society*. URL: https://glossary.ametsoc.org/wiki/Froude_number.
- [5] P. Ditlevsen and S. Ditlevsen. “Warning of a forthcoming collapse of the Atlantic meridional overturning circulation”. 2023. P. 4254. URL: <https://www.nature.com/articles/s41467-023-39810-w>.
- [6] C. Garrett. “A stirring tale of mixing”. 1993. Pp. 670–671. URL: <https://www.nature.com/articles/364670a0>.
- [7] E. H. Iribarne. “Transport properties of internal gravity waves”. en. PhD thesis. Ecole normale supérieure de lyon - ENS LYON, Oct. 2015. URL: <https://theses.hal.science/tel-01244324> (visited on 11/30/2023).
- [8] C. Koudella. “Ondes internes de gravité en fluide stratifié: instabilités, turbulence et vorticit   potentielle”. fr. PhD thesis. Ecole normale supérieure de lyon - ENS LYON, Apr. 1999. URL: <https://theses.hal.science/tel-00005960> (visited on 11/30/2023).
- [9] N. Kuzmina and V. Zhurbas. “Effects of Double Diffusion and Turbulence on Interleaving at Baroclinic Oceanic Fronts”. 2000. Boston MA, USA. American Meteorological Society. Pp. 3025–3038. URL: https://journals.ametsoc.org/view/journals/phoc/30/12/1520-0485_2000_030_3025_eoddat_2.0.co_2.xml.
- [10] M. Le Bars. “Numerical study of the McIntyre instability around Gaussian floating vortices in thermal wind balance”. 2021. American Physical Society (APS). URL: <http://dx.doi.org/10.1103/PhysRevFluids.6.093801>.
- [11] M. Le Bars, B. Favier, and D. Lemasquerier. “La Grande Tache rouge de Jupiter... en laboratoire!”. 2021. Pour la Science. Pp. 24–33.
- [12] J. C. McWilliams. “Submesoscale currents in the ocean”. 2016. P. 20160117. URL: <https://royalsocietypublishing.org/doi/abs/10.1098/rspa.2016.0117>.
- [13] T. Meunier et al. “Tracer Stirring around a Meddy: The Formation of Layering”. 2015. Boston MA, USA. American Meteorological Society. Pp. 407–423. URL: <https://journals.ametsoc.org/view/journals/phoc/45/2/jpo-d-14-0061.1.xml>.
- [14] J. Pedlosky. “The spin up of a stratified fluid”. 1967. Cambridge University Press. Pp. 463–479.
- [15] P. Richarson. “Tracking Ocean Eddies”. 1993. Pp. 261–271.
- [16] *Site de l’IRPHE : irphe.univ-amu.fr*. URL: <https://irphe.univ-amu.fr/fr/public/basic-page/presentation>.
- [17] S. Smirnov, J. Pacheco, and R. Verzicco. “Laboratory-numerical studies of stratified spin-up flows”. 2008. URL: <https://doi.org/10.1007/s10652-008-9087-2>.

- [18] B. R. Sutherland. *Internal gravity waves*. Cambridge University Press, Sept. 2010. ISBN: 9780521839150. URL: <https://www.cambridge.org/fr/universitypress/subjects/earth-and-environmental-science/atmospheric-science-and-meteorology/internal-gravity-waves?format=HB&isbn=9780521839150>.
- [19] E. Yim and P. Billant. “Analogies and differences between the stability of an isolated pancake vortex and a columnar vortex in stratified fluid”. 2016. Pp. 732–766.

Abstract

In this report, we present theoretical, numerical and experimental approaches to better understand instabilities generated by a sphere rotating in a stratified fluid. Base flow equations are solved analytically for velocity and density. Internal gravity waves are as well studied. The experimental setup is composed of a cylindrical rotating tank filled by stratified salt water and containing a vertical rotating axis on which is placed a solid sphere. The apparatus is placed on a rotating table in order to simulate a Coriolis effect. Conducted experiments include velocity settling and instabilities measurements. Period and normal mode of the instability are estimated for the equatorial instability. Results for polar instability are not conclusive due to technical issues.

Keywords

Stratified fluid ; Geophysical flow ; Vortex instability ; PIV ; Mediterranean Eddies